ORIGINAL ARTICLE

Impact of loading rate on the mechanical behavior of jointed rock

Tao Wang [ORCID] · **Derek Elsworth** · **Yunlong He** ·
Xianyu Zhao · **Suifeng Wang** · **Dapeng Xu** ·
Ming Lei

Abstract   The impact of loading rate is a vital issue in the study of the time-dependent behavior of rock masses. A sample containing a single inclined joint is represented by the particle flow code and used as an analog to examine the rate-dependent behavior of jointed rock. A series of numerical triaxial compression tests are completed at various loading rates on specimens containing this single joint inclined at 30°, 45°, and 60° with respect to the orientation of the confining stress of 5 MPa. Observations are recovered for the evolution of stress–strain, deformation and energy release together with resulting failure mode. Rate sensitivities of four parameters defining a smooth joint model (normal stiffness, shear stiffness, stiffness ratio and friction coefficient) are used to represent observed response. We find that competition between mechanical damping and inertial force results in the strain rate effect and that the peak strength of the rock specimens increases with increasing loading rate. The step-wise form of both the stress–strain and kinetic energy can be used as indicators of the onset of dynamic failure. These numerical experiments are consistent with observations from laboratory experiments on identical samples where rate effects in the jointed rock are accentuated over those apparent in intact rocks. Change in the loading rate has a significant effect on the failure mode for specific joint angles relative to the confining stress. The joint friction coefficient is the main rate dependent factor controlling behavior and is an important factor in defining the significance of loading rate effects.

Article Highlights

- A series of numerical triaxial compression tests are completed at various loading rates on specimens containing this single joint inclined at 30°, 45°, and 60°.
- Rate sensitivities of four parameters defining a smooth joint model (normal stiffness, shear stiffness, stiffness ratio, and friction coefficient) are used to represent the observed response.
- These numerical experiments are consistent with observations from laboratory experiments on identical samples where rate effects in the jointed rock are accentuated over those apparent in intact rocks.

T. Wang (✉) · Y. He · X. Zhao · S. Wang · D. Xu · M. Lei
State Key Laboratory of Water Resources Engineering
and Management, Wuhan University, Wuhan 430072,
China
e-mail: htwang@whu.edu.cn

D. Elsworth
Energy and Mineral Engineering and Geosciences, G3
Center and EMS Energy Institute, Penn State University,
University Park, PA, USA
e-mail: elsworth@psu.edu

1 Introduction

Loading rate exerts a significant influence on the mechanical properties of rock containing discontinuities rendering rock masses more sensitive to these effects than intact rock. This dependency results from the role of inertial forces at ultra-high rates (Blanton 1981) and impacts of friction and non-linear deformation on surfaces at low rates (Dieterich 1978). Loading rates vary over a spectrum of timescales, incorporating creep, standard compression, earthquake, dynamic impact and explosive loadings in order of monotonically increasing rates. In a general manner, loading rate regimes may be divided among static loading, quasi-dynamic loading, and fully-developed dynamic loading as rates progressively increase, as shown in Table 1. Increasing loading rates increase the apparent strength of intact rock (e.g., Swan et al. 1989; Lajtai et al. 1991; Li et al. 2013) with an abrupt increase in strength at threshold loading rates (Olsson 1991; Qi et al. 2009).

Coefficients of friction of joint surfaces are sometimes considered to be constant, but are typically both time-dependent (Dieterich 1972; Schneider 1977) and rate-dependent (Dieterich 1978). "Stick–slip" is intrinsically associated with rate-weakening effects of friction on rock surfaces (Jaeger et al. 2007) and rate-and-state friction (Scholz 1998) provides a suitable representation for this and its elevated impact on interfaces relative to intact rock (Fahimifar 1996, 1997; Fahimifar and Soroush 2005).

Table 1 Threshold values of strain rates separating states of dynamic, quasi-dynamic and static loading

References	Strain rate $\dot{\epsilon}/s^{-1}$		
	Static	Quasi-dynamic	Dynamic
Blanton (1981)	–	$10^{-1} \sim 10^1$	–
Li et al. (2013)	$10^{-4} \sim 10^1$	–	$10^1 \sim 10^4$
Logan (1970)	$10^{-5} \sim 10^{-2}$	$10^{-2} \sim 10^2$	$> 10^2$
Olsson (1991)	$10^{-4} \sim 10^1$	–	$10^1 \sim 10^3$
Qi et al. (2009)	$10^{-4} \sim 10^{-2}$	$10^{-2} \sim 10^2$	$> 10^2$
Sierakowski (1985)	$10^{-4} \sim 10^{-1}$	$10^{-1} \sim 10^0$	$> 10^2$
Tarasov (1990)	$10^{-8} \sim 10^{-3}$	–	$10^{-2} \sim 10^0$

Distinct element methods (DEM) have been widely used as a powerful tool to investigate the mechanical behavior (strength, deformation and failure processes) of rocks and jointed rock masses (Potyondy and Cundall 2004). Jointed rock masses can be described in such granular mechanics models using a Synthetic Rock Model (SRM). Such SRM models (Ivars et al. 2011) consider mechanical behaviors as a combination of intact rock and joints. Particles are bonded by parallel-planes to simulate the behavior of intact rock (Wang et al. 2014) with a contact model incorporating bonded particles (BPM). However, preexisting joints in a rock mass are discontinuous and may slip along the locus of their planes—this can be enabled with a Smooth Joint Model (SJM) which neglects the geometric positions of the local particles, to allow smooth gliding along a linear surface that transects individual particles, to correctly simulate the behavior of smooth sliding along the joint plane (Huang et al. 2015). The SJM has proven effective in predicting the mechanical behavior of rock joints (e.g., Bahaaddini et al. 2016; Wang et al. 2017; Zhang et al. 2017; Chen et al. 2018; Huang et al. 2019; Gao et al. 2020), despite its imperfections (Mehranpour and Kulatilake 2017). The coefficient of friction in the SJM is assumed to be constant, but may accommodate the roughness of the joint surface where the parameters are modified according to, for example, a Barton-Bandis failure criterion (Chiu et al. 2013; Lambert and Coll 2014). Loading rate effects in synthetic rock mass models (SRM) are simultaneoulsy influenced by both BPM and SJM effects. Strain rate effects for BPMs may be accommodated by 'step strain rates' (Zhang and Wong 2014).

The effect of loading rate of the mechanical properties of rock materials is an important issue. At present, there are many studies on loading rate effects of intact rock, while those addressing loading rate effects in jointed rock masses are relatively rare. The following reports triaxial compression experiments conducted at various loading rates to define the impacts of loading rate on deformation and failure behavior. These observations are used to calibrate a numerical SRM model for a cylindrical core transected by a single inclined through-going joint. Rate sensitivity of the smooth joint model parameters, under different loading rates, are explored to define the observed response and to deconvolve behavior.

2 Physical and numerical models of fractured specimens

Compression experiments are completed on cylindrical samples containing through-going fractures where deformation is measured under constant loading rates. These are used to calibrate virtual models of identical geometry.

2.1 Physical experiments

Figure 1 shows the physical samples of both intact and jointed rocks. The results for deviatoric stress versus total axial strain for the physical tests are shown in Fig. 2. These are derived from triaxial compression tests on specimens at a single confining pressure of 5 MPa. To maximize reproducibility (Zou et al. 2022), the physical specimens comprise rock-like materials of water:sand:cement in the proportion 0.169:0.365:0.466 by weight. These specimens are prepared to dry. A single artificial fracture is saw-cut in each specimen to produce a persistent unfilled joint that transects the center of the different samples at dip orientations of 30° and 45° with respect to the horizontal (orientation of confining stress). Triaxial compression tests are completed for intact specimens under different confining pressures. By comparison, it can be seen that the mechanical properties of the material are similar to that of brittle sandstone. Due to the limitation of experiment conditions, there was no physical experiment of dip orientation of 60° at
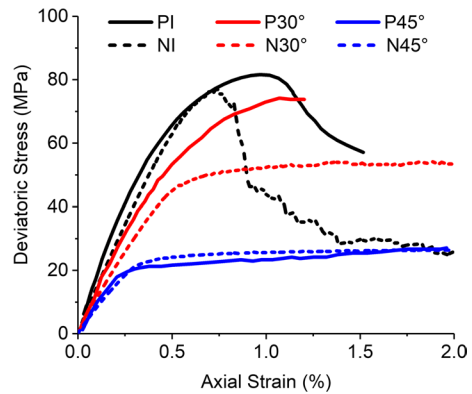
Fig. 2 Stress–strain curves for physical and numerical tests, Solid lines represent the results of physical tests (P) and dotted lines represent the results of numerical simulations (N). The results for the intact rock are displayed as black lines (I), and the results for jointed rock with joint angles of 30° and 45°are displayed as red (30°) and blue lines (45°), respectively

confining pressure of 5 MPa. However, the physical and numerical investigations of dip orientation of 60° at confining pressure of 10 MPa in the author's previous study can be used for reference (Hu et al. 2018).

The transected specimens were then reassembled and fixed with adhesive tape along the joint trace to retain both ends of the jointed cylindrical specimen parallel. The three models of Fig. 1 are all post-experiment with the red dashed lines representing preexisting joints. The samples are loaded in the axial direction at a rate of 2 kN/s. The density of the specimens is 2085 kg/m^3. The numerical experiments replicate

Fig. 1 Physical experimental models of intact and jointed rocks (red dashed lines represent preexisting joints; blue dashed circles represent shear bands)
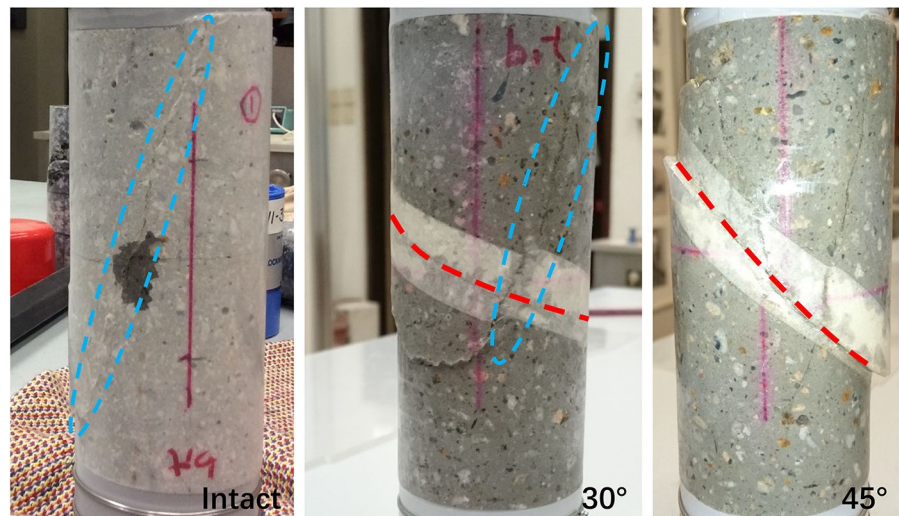
exactly the physical samples and experiments. The (numerical) jointed rock models with three dip angles of 30°, 45° and 60° together with intact rock are tested at five loading rates (0.05/s, 0.5/s, 5/s, 10/s, and 15/s) and mirror the triaxial compression tests conducted at a confining stress of 5 MPa.

2.2 Virtual experiments

Virtual experiments are conducted to calibrate the response against the physical experiments. An SJM model is used to overcome the inherent roughness of the particulate interface and to simulate the behavior of a smooth interface regardless of local particle sizes and orientations (Ivars et al. 2011). The SJM has two modes—unbonded or bonded—as selected in simulating the behavior of a frictional or bonded interface. The bonded mode employs a Coulomb sliding law to incorporate friction and cohesion after breakage of the cohesive bond. The combination of the BPM and the SJM makes the SRM approach a valid pathway to characterize properties and behavior of jointed rock masses.

2.2.1 Intact rock specimen

An intact rock specimen was created by BPM using the method of Potyondy and Cundall (2004). A cylindrical vessel is generated using six walls, two additional platens at the top and bottom and four cylindrical surfaces surrounding the sample. The height of the vessel is 122.7 mm, and the diameter is 51.74 mm. In order to retain the representativeness, precision and the efficiency of the PFC calculation, the size of particles is retained less than 1/20th of the diameter of the cylinder with a uniform particle size distribution (minimum radius (R_{min}) of 1.2 mm) and with a fixed ratio of maximum radius to minimum radius (R_{max}/R_{min}) of 1.66. The selection of particle sizes is founded upon the established guidelines suggested by the International Society for Rock Mechanics (ISRM) with regards to best practices in experimental procedures (Fairhurst and Hudson 1999). The total number of spherical particles comprising the numerical specimen is 12,546.

The assembly of frictionless particles is compressed at a small isotropic stress until the particles are compacted, and the contact forces have equilibrated. Finally, parallel bonds are applied between all particles in relative proximity to each other and the specimens of intact rock completed.

2.2.2 Jointed rock specimen

Intact specimens are transected by a single joint passing through the center of the virtual (numerical) specimen. The dip angle and dip direction of the joint is an octagonal disk passing through the joint center and is oriented parallel to the joint surface (Fig. 3). The radius of the disk (blue polygon) is set at 100 mm to ensure that it fully transects the specimen. To retain the smooth behavior of the joint, the thickness of the polygon is set intermediate between the minimum and maximum particle radius. The sample is transected by this joint at inclinations of 30°, 45°, and 60°, as shown in Fig. 3. The SJM model is activated in all particles intersected by the disk instead of a parallel bond model.

Fig. 3 Numerical specimens of intact and jointed rock. The dip inclination of the joint (θ) is measured from the horizontal

Intact   θ=30°   θ=45°   θ=60°
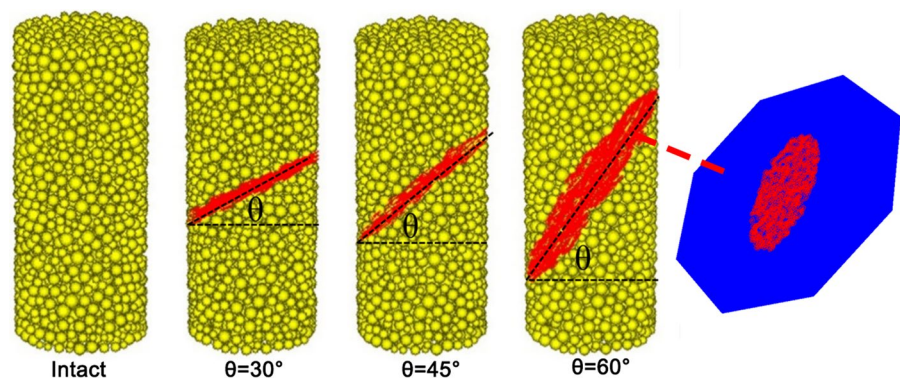
2.3 Calibration of jointed rock specimens

Loading is completed in two phases to replicate the conditions of our physical triaxial compression tests. The first phase is a seating phase in which the confining stress is uniformly set to 5 MPa by using the servo-loading mechanism. The second phase is the loading phase where the confining pressure is maintained, and the sample loaded in the axial direction at the prescribed velocity. A servo-loading mechanism is implemented to achieve the desired loading schedule.

The parallel bond model was calibrated first, to match the results of the experiments conducted on the intact physical specimens. Contact stiffness was first varied to match the observed Young's modulus of the intact rock. This was achieved by setting the bond strength to a large value and then matching the Poisson ratio by varying the normal and shear stiffnesses. Peak strength was then matched by varying the parallel bond normal and shear strengths. The calibrated values of the microscopic parameters, including Young's modulus (E_c), ratio of particle normal to shear stiffness (k^n/k^s), particle coefficient of friction (μ_c), parallel bond Young's modulus ($\overline{E}_c$), ratio of parallel bond normal to shear stiffness ($\overline{k}^n/\overline{k}^s$), parallel bond normal strength ($\tilde{\sigma}_c$) and shear strength ($\overline{\tau}_c$) are listed in Table 2. Zhang and Wong (2014) suggests that the magnitude of the stepped strain rate should be approximately 10^{-8}/step—the strain rate used to calibrate the parameters is 0.5/s, and the timestep is 1.938×10^{-7} s/step in this study.

The calibration of the SJM is then completed for the sample with a fracture angle of 45°. After inclusion of the fracture, the properties of the SJM are inherited from the parallel bond model. Unlike the parallel bond model, the shear strength of the smooth joint model follows the Mohr failure

criterion, defined by the cohesion (c_b) and friction angle (ϕ_b) (Duan et al. 2016). Considering that the joints were introduced as saw cuts, the SJM model in this study is set as unbonded. For this, the normal strength (σ_c), cohesion (c_b), dilatancy angle (ψ) and friction angle (ϕ_b) are all set to zero. The calibrated values of other microscopic parameters of the SJM, viz. the radius multiplier ($\overline{\lambda}$), the normal and shear stiffness ($\overline{k}^n$ and $\overline{k}^s$), and the friction coefficient (μ) are listed in Table 2.

Triaxial compression is applied to both physical and numerical tests. Comparison between the stress–strain curves of the physical tests and numerical tests are as shown in Fig. 2.

In previous studies of parameters of the SJM on the mechanical behavior of joint rock (Hu et al. 2018), we concluded that after the micromechanical properties were calibrated at joint dip angles of 45°, the discrepancy could be observed in the case of 30° and 60°. This can be explained through two observations: (1) The micro parameters, except joint orientation, for all the cases were the same while the properties of the artificial joint, including roughness, friction coefficient, and stiffness, were difficult to retain consistency in different specimens; (2) Different from the physical experiments, the application of confining pressure in the simulations via rigid walls created a non-uniform stress distribution along the surface of the specimen. Therefore, it isn't easy to achieve complete agreement between the physical and numerical experiments in some cases. It is worth noting that the same transition of stress–strain curves from brittle to ductile due to the change in joint orientation was observed in both the experimental and numerical results. Considering that this discrepancy will not affect the research of variation rule of mechanical behavior of jointed rock in this paper the recovered numerical

Table 2 Micromechanical properties of particles and contacts

Particle	Value	Parallel bonded model	Value	Smooth Joint Model	Value
E_c (GPa)	12	$\overline{E}_c$ (GPa)	12	$\overline{k}^n$ (GPa/m)	1260
k^n/k^s	1.5	$\overline{k}^n/\overline{k}^s$	1.5	$\overline{k}^s$ (GPa/m)	840
μ_c	0.5	$\tilde{\sigma}_c$ (MPa)	75 ± 40	μ	0.15
R_{max}/R_{min}	1.66	$\overline{\tau}_c$ (MPa)	75 ± 40	σ_c, c_b (MPa)	0
R_{min} (mm)	1.8	$\overline{\lambda}$	1.0	ψ, ϕ_b (deg)	0
ρ (kg/m^3)	2085.16				

mesoscopic parameters may be considered reasonable and reliably used in the subsequent numerical simulation studies.

3 Effects of loading rate on the macro-mechanical properties

Loading rates applied by the walls are controlled by a servo-loading mechanism, as described in our prior work (Wang et al. 2016; Hu et al. 2018). The confining stress is also controlled by a servo-mechanism where the velocity of the wall is set to be equal and opposite to maintain the specified pressure as,

$$\frac{|P^w - P^t|}{P^t} \leq \varepsilon_p \tag{1}$$

where P^w is the current pressure on the wall, P^t is the target pressure and ε_p is the equilibrium-pressure tolerance. A velocity boundary condition is used to apply the stress with the loading velocity controlled by the axial strain rate and the axial length of specimens as,

$$|v| = \frac{1}{2}\dot{\varepsilon}_a h_a \tag{2}$$

where, v is the loading velocity of the wall, $\dot{\varepsilon}_a$ is the axial strain rate and h_a is the axial length of specimens.

A strain rate of 0.5/s is used to maintain the quasi-static loading state in the previous calibration tests. The strain rate used in the numerical simulation is larger than that in the physical test. The calibration tests require a strain rate to maintain the quasi-static loading state. The value of 0.5 is appropriate because the stepped strain rate is of the order of 10^{-8} which can maintain stability in the explicit dynamic calculation used in PFC. To study the effect of loading rate on the response of jointed rock masses we select five designated strain rates of 0.05/s, 0.5/s, 5/s, 10/s, 15/s spanning static to fully dynamic conditions (Table 1). Except for the loading rates, all other mechanical conditions are the same as the calibration tests.

3.1 Effect on stress–strain response

The stress–strain curves of all specimens at the five loading rates are as shown in Fig. 4. Each curve terminates at an axial strain of $\varepsilon=2\%$. As indicated in Fig. 4, the loading rate has a clear impact on the stress–strain curves. For intact specimens, as shown in Fig. 4a, peak strength increases with an increase in loading rate despite no significant change in the

Fig. 4 Stress–strain curves of intact and jointed specimens under various strain rates (red circle indicates the yield point from linear to nonlinear)
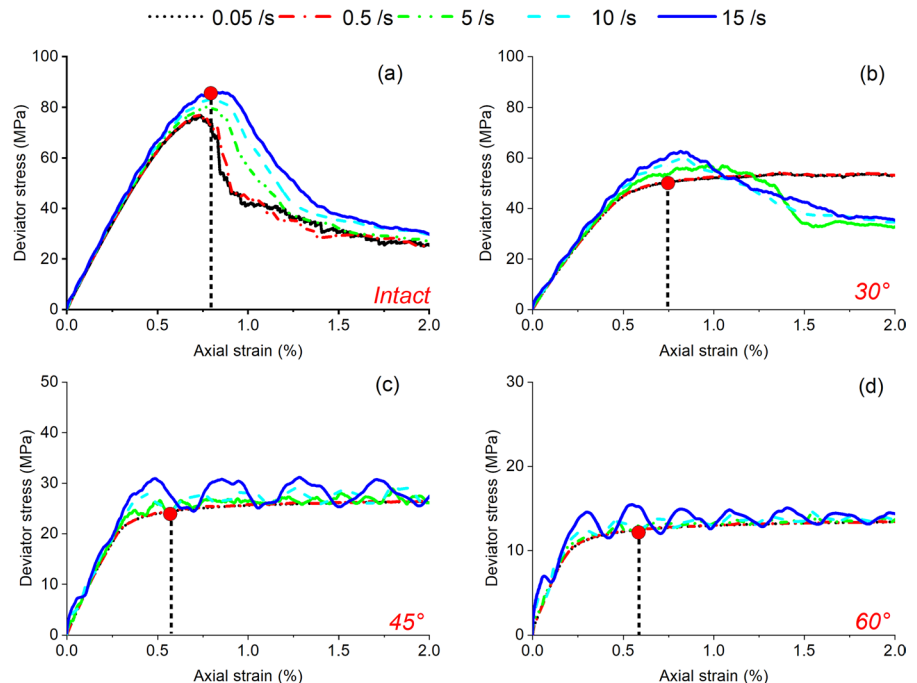
deformation modulus. The post-peak stress–strain curve for loading at 0.05/s is steep. As the loading rate increases, the slope of the post-peak stress–strain curves become progressively shallower. This implies that the increase in loading rate leads to a transition from brittle failure to strain softening. These results are consistent with the conclusions of Zhang and Wong (2014) and Jackson et al. (2008). They found that both ductility and peak stress increase with an increase in strain rate from observations of rate dependent loading of intact rock.

We find that the stress–strain curves of the intact specimens have a clear peak at maximum strength and exhibit strain softening in the post-peak phase. By contrast, when the jointed specimens slip along the joint surface, the stress–strain curves have no apparent peak, and the post-peak phase is pure due to shear sliding without obvious peaks. As exhibited in Fig. 4b, when the strain rate is below 5/s, the stress–strain curves of the jointed specimens with a 30° joint become shallower as they pass through the elastic phase. The transition from the elastic stage to shear sliding is represented by the peak strength of stress–strain curves (Hu et al. 2016) (red circles

shown in Figs. 4b, c, d). When the loading rate is greater than 5/s, the stress–strain curves mimic the response of intact specimens with a clearly defined peak strength and with a post-peak phase of strain softening.
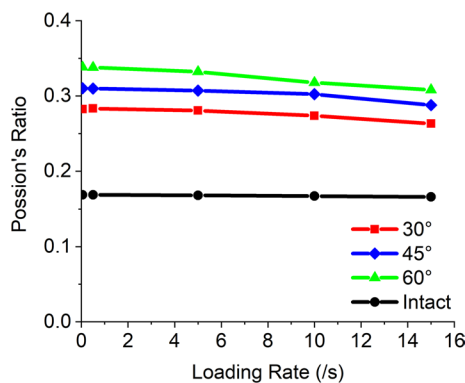
As shown in Figs. 4c, d, when the strain rate is below 5/s, the stress–strain curves of the jointed specimens with joint inclinations of 45° and 60° are similar to the response to that for a joint at an inclination of 30°. However, with an increased inclination of the joint, the stress threshold for this transition decreases. When the strain rate is greater than 5/s, the stress–strain curves appear conspicuously step-like—a typical characteristic of dynamic loading. By contrast, Fig. 4a, b show that when the strain rate is greater than 5/s, a subtle step-wise feature appears in the stress–strain curves. Zhang and Wong (2014) also observed a similar phenomenon in their numerical experiments under uniaxial compression.

The peak strength and elastic modulus of each specimen in Table 3 are obtained from the stress–strain curves in Fig. 4—all increased percentages are calculated relative to behavior at a strain rate of 0.05/s. With the increase in loading rate, peak

Table 3 Peak strength and elastic modulus recovered from triaxial compression tests
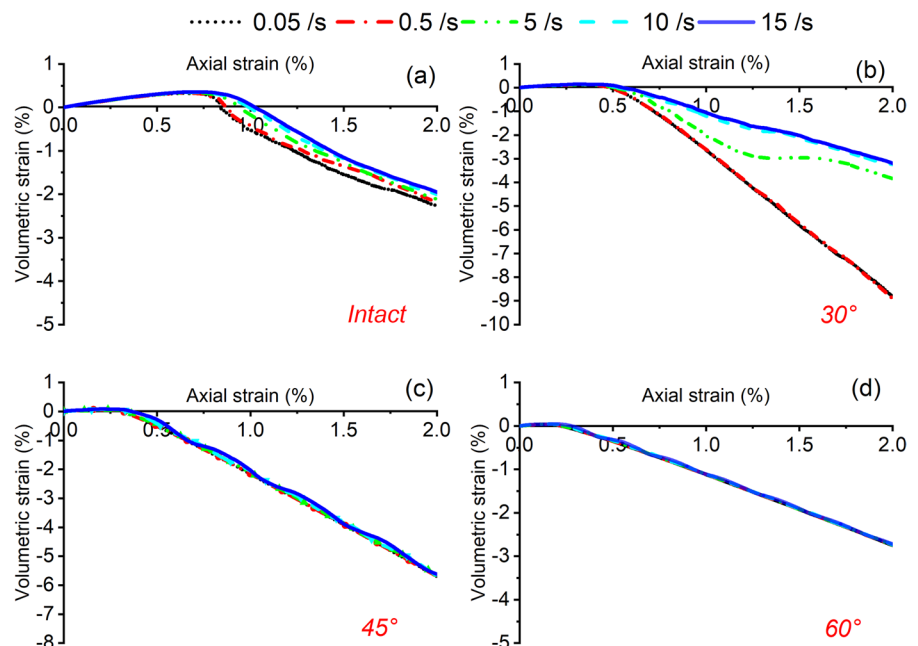
Joint angle	Specimen number	Strain rate	Peak strength (Mpa)	Elastic modulus (Gpa)
Intact	1	0.05	81.9	13.6
	2	0.5	82.06 (+0.2%)	13.62 (+0.15%)
	3	5	85.45 (+4.33%)	13.79 (+1.4%)
	4	10	88.35 (+7.88%)	13.94 (+2.5%)
	5	15	91.16 (+11.31%)	14.13 (+3.9%)
30°	6	0.05	58.86	10.25
	7	0.5	59.34 (+0.82%)	10.25 (+0.00%)
	8	5	62.02 (+5.37%)	10.5 (+2.44%)
	9	10	65.5 (+11.28%)	10.76 (+4.98%)
	10	15	67.7 (+15.02%)	11.25 (+9.76%)
45°	11	0.05	31.35	7.84
	12	0.5	31.54 (+0.61%)	7.87 (+0.38%)
	13	5	33.87 (+8.04%)	8.1 (+3.32%)
	14	10	34.41 (+9.76%)	8.36 (+6.63%)
	15	15	36.17 (+15.37%)	8.72 (+11.22%)
60°	16	0.05	18.4	5.75
	17	0.5	18.55 (+0.82%)	5.78 (+0.52%)
	18	5	19.24 (+4.57%)	5.99 (+4.17%)
	19	10	19.6 (+6.52%)	6.71 (+16.7%)
	20	15	20.44 (+11.09%)	7.13 (+24%)

strength and elastic modulus of each group of specimens change in different modalities. As the loading rate increases to 15/s, the peak strength increases by 11.31% and the elastic modulus increases by 3.9% relative to the case of the intact specimen. They increase 15.02% and 9.76% respectively for the case of a 30° joint, 15.37% and 1.22% respectively for a 45° joint and 11.09% and 24% respectively for the 60° joint. This illustrates that for the case of a 45° joint, the change in peak strength with an increase in the loading rate has the greatest increase in strength and modulus. For a joint at 60°, the elastic modulus is

more sensitive to loading rate than the peak strength. These loading-rate-induced changes in strength are new to the literature.

3.2 Effect on deformation characteristics

Under the various loading rates, the deformation behavior of rock specimens containing a joint displays clear regularity. As shown in Fig. 5, when the loading rate is increased from 0.05/s to 15/s, the reduction in Poisson's ratio of the jointed specimens for the 30° (6.81% reduction), 45° (7.23% reduction) and 60° joints (8.94% reduction) is larger than that of the intact specimen (1.7% reduction). The more steeply inclined the joint, the larger the deformation of the rock mass and the larger the Poisson's ratio. This behavior indicates that, for a low loading rate, the rate of change of lateral strain becomes greater than the rate of change in axial strain—due to a slight dilation at the initiation of sliding.

The effect of loading rate on the deformational behavior of jointed specimens in which joint sliding is a leading cause of later-stage deformation is pronounced. As shown in Fig. 6a, when the loading rate is 0.05/s or 0.5/s, the deformation style of the intact specimens changes little, and the volume strain curves exhibit little variation. As the loading rate continues to increase, the volume strain of the intact specimens

Fig. 5 Change in Poisson's ratio of intact and jointed specimens under various loading rates

Fig. 6 Volumetric strain versus axial strain curves of intact and jointed specimens under various loading rates

rises steeply as the increased loading rate restricts the change of lateral deformation. Similar results have also been observed by Fahimifar (1996) who found that increased strain rate both decreases the reduction in volume strain and joint closure.

As shown in Fig. 6b, when the loading rate is either 0.05/s or 0.5/s, shear sliding occurs on the joint surface of the specimens containing a joint at 30° and the evolutions of volume strain are almost coincident. As the loading rate continues to increase, the volume strain decreases. We speculate that the lateral strain is fully manifest at low loading rates where the volume of the specimens expands with time and the volume strain increases. However, with an increase in the loading rate, the sensitivity of the response to lateral strain gradually decreases, and the development of the lateral strain is restricted. Hence, the rate of volume expansion gradually reduces with an increase in the loading rate.

As shown in Fig. 6c, d, when the joint dip is 45° or 60°, the evolution of volume strain at various loading rates is again almost coincident. This form of deformation is mainly related to the failure mode of the jointed specimens. Shear sliding occurs along the joint surface at various loading rates when the joint angle is 45° or 60°, so the volume expansion of the jointed specimens retains the same behavior. Moreover, the lateral deformation is also limited by the joint angle since the higher inclination joint decreases the slope of the volume strain curve.

3.3 Effect on failure modes

The breakage of bonded contacts between particles in PFC (Wang et al. 2016) acts as a proxy for the failure state of the virtual samples representing the rock mass. Fracturing results when normal or shear contact forces between the particles in the rock specimens exceed the prescribed normal stress or shear stress intensity thresholds (strengths). In Fig. 7, the samples are sliced by a zone of thickness equal to one-fifth of the sample radius and cut through the center of the specimens across the radius. The information contained in the zone, such as evolution of cracks, contact force chains and smooth joint contact is projected onto this plane. Black dots represent tensile cracks, light red dots correspond to the shear cracks, light orange background network shading represents contact force chains (the thickness of the force chain

corresponds to the magnitude) and the light blue streaks indicate smooth joint contacts.

The failure modes observed in the jointed rock masses can be classified into three modes: axial splitting (splitting by fracture through intact rock), sliding (sliding along the pre-existing joint plane), and mixed mode failures (mixed failure in splitting and sliding modes) (Hu et al. 2016). As shown in Fig. 7, with an increase in loading rate, splitting failure mainly occurs in the axial direction. A large number of microcracks are primarily distributed proximal to the spatial focusing force chains in which the contact force is large. We speculate that the contact force can be transmitted even if there is no bonding force between the particles after the breakage of parallel bonded contacts—due to frictional transmission. When the joint dip is 30° and the strain rate is 0.05/s or 0.5/s, shear sliding mainly occurs along the joint surface and the small number of tensile and shear cracks are evenly distributed. As the loading rate continues to increase, more cracks appear at the top and bottom of the samples—at the platen contact. This implies that if the loading rate is sufficiently large, the contact forces at both ends cannot transfer sufficiently rapidly (inertial constraint) to other parts of the sample and therefore crack formation concentrates at both ends of the specimens—principally represented by mixed mode failure (Fig. 7c, d). The presence of a joint surface requires that the energy passing from both ends of the sample to the joint surface is converted into frictional energy by shear sliding. It is difficult to accumulate significant strain energy, so cracks adjacent to the joint surface have difficulty in growing and extending. When the joint dip is 45° or 60°, the failure mode of the specimens is similar to that for 30°, but an increase in the loading rate has less influence on the failure pattern. Compared with the case for 30°, the angle between the axial load and the joint surface is smaller and sliding on the joint surface is more easily induced. The failures are all in sliding mode when the joints are at 45° or 60° (Fig. 7e, f), although the intact specimen split axially in tension (Fig. 7a, b).

Monitoring the number of microcracks that initiate is an effective way to describe microcrack development and the initiation of rupture. A tensile or shear microcrack is generated corresponding to the failure state breaking a parallel bond. Figure 8 shows the number of microcracks in specimens subjected to
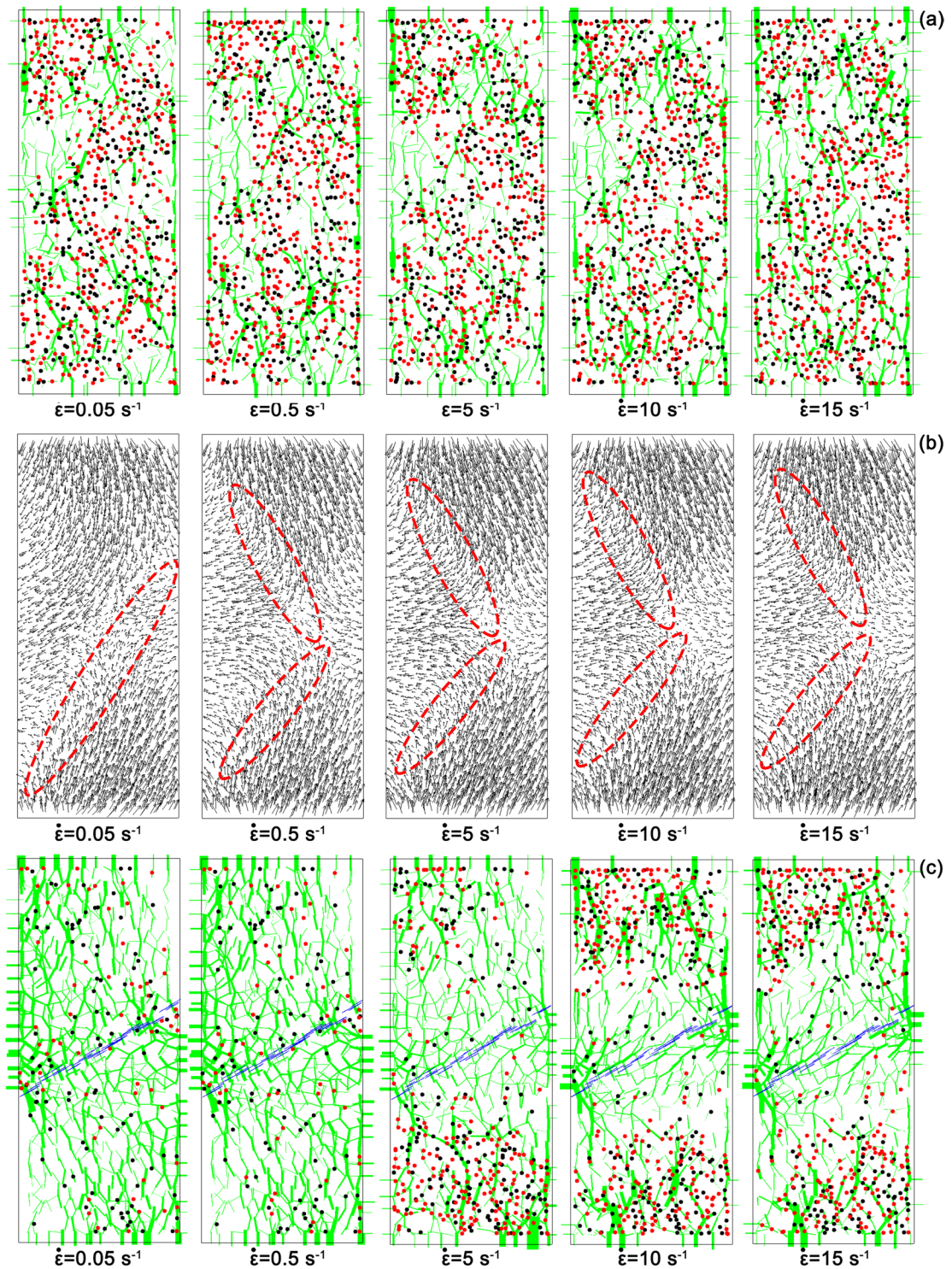
Fig. 7 Crack propagation and displacement distribution in intact and jointed specimens at various loading rates (**a**, **b**-intact; **c**, **d**-30°; **e**, **f**-45°; **g**, **h**-60°; the red dots represent tensile cracks, the black dots represent shear cracks, the yellow chains represent contact forces and blue dashed lines represent smooth joint contacts)
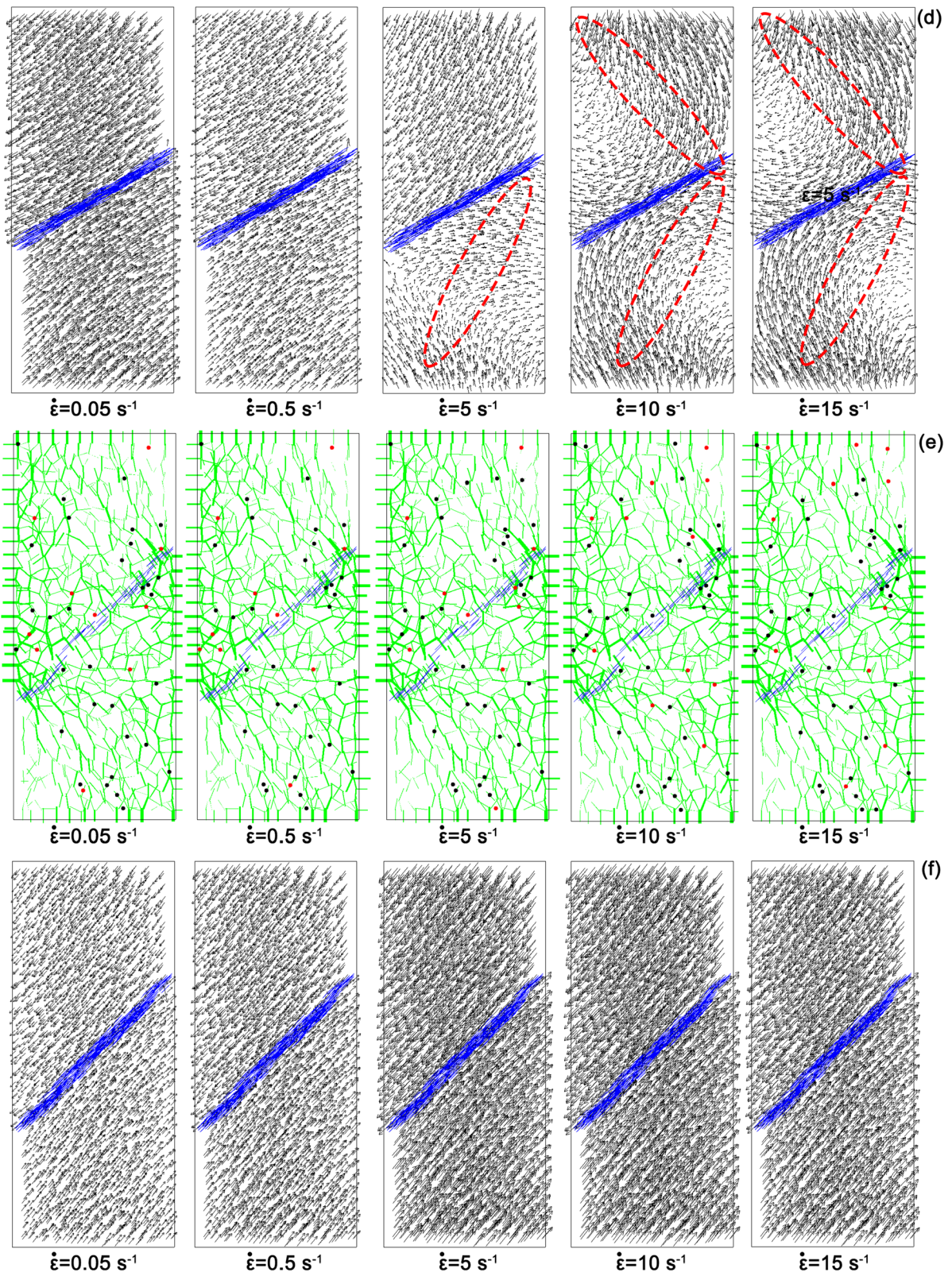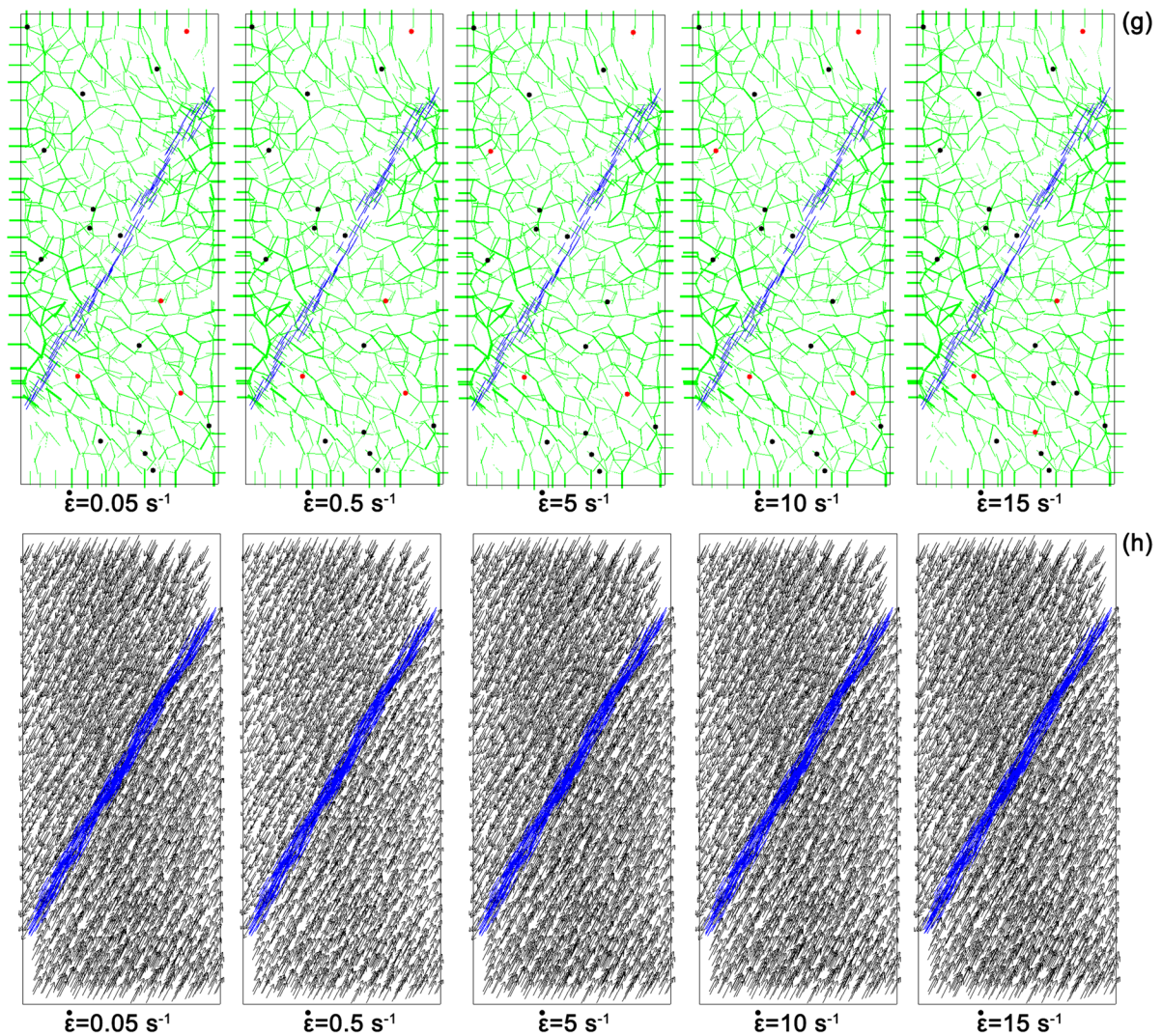
Fig. 7 (continued)

$\dot{\epsilon}$=0.05 s^{-1} $\dot{\epsilon}$=0.5 s^{-1} $\dot{\epsilon}$=5 s^{-1} $\dot{\epsilon}$=10 s^{-1} $\dot{\epsilon}$=15 s^{-1}

$\dot{\epsilon}$=0.05 s^{-1} $\dot{\epsilon}$=0.5 s^{-1} $\dot{\epsilon}$=5 s^{-1} $\dot{\epsilon}$=10 s^{-1} $\dot{\epsilon}$=15 s^{-1}

Fig. 7 (continued)

the five different loading rates. The three curves correspond to the total number of microcracks (T_o), the number of tensile microcracks (T_e) and the number of shear microcracks (S) and are shown for each loading rate. The relationship between these metrics is $T_o = T_e + S$ with Fig. 8 revealing the following effects of the loading rate on crack intensity.

The number of cracks is closely related to the modes of both shear sliding and axial splitting failure. As shown in Fig. 8a, b, an increase in the loading rate results in a clear growth of the number of microcracks. The number of microcracks reflects the degree of damage of the compressed rock. When the loading

rate is 0.05/s or 0.5/s, the number of shear microcracks that develop exceed the number of tensile microcracks for the 30° joint. The specimens mainly slide in shear along the joint surface. For intact specimens the number of shear microcracks is nearly equal to the number of tensile microcracks. When the loading rate exceeds 5/s, the number of tensile microcracks are greater than the number of shear cracks and the failure mode is by axial splitting failure both for intact specimens and for the case of the frictionally constrained 30° joint. Figure 8c, d show that when the joint dip is 45° or 60°, there are more shear microcracks than tensile microcracks under

Fig. 8 Number of microcracks in intact and jointed specimens under various loading rates
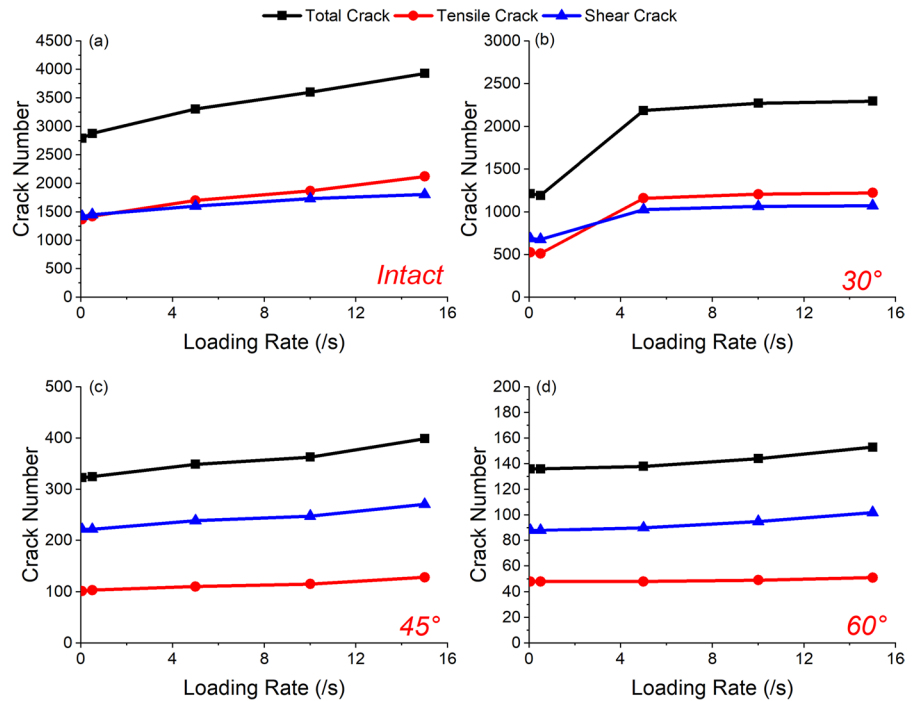
the various loading rates corresponding to the failure mode of shear sliding.

3.4 Energy response under different loading rates

In PFC, the energy is partitioined as follows (Itasca 2008): Boundary energy (E_w) is the accumulated work of the forces and moments done by walls in the particle model. For each wall, the force is expressed as F_i and the moment is expressed as M_3. The corresponding displacement is ΔU_i and the rotation angle is θ_3 and this occurs on a total number of walls, N_w. Thus, boundary energy can be expressed as:

$$E_w = \sum_{N_w} (F_i \Delta U_i + M_3 \theta_3) \tag{3}$$

Bond energy (E_{pb}) is the energy stored in the bond. For each bond contact, the normal force is $\overline{F}_i^n$, the shear force is $\overline{F}_i^s$ with a moment of $\overline{M}_3$; the normal stiffness is $\overline{k}^n$, the shear stiffness is $\overline{k}^s$ and the moment of inertia of a contact area is I. The bonded area of the contact is A. The number of bonded contacts is N_w. Thus, bond energy can be expressed as:

$$E_{pb} = \sum_{N_{pb}} \left(\left|\overline{F}_i^n\right|^2/(A\overline{k}^n) + \left|\overline{F}_i^s\right|^2/(A\overline{k}^s) + \left|\overline{M}_3\right|^2/(I\overline{k}^n) \right)/2 \tag{4}$$

Frictional energy (E_μ) is the energy dissipated due to frictional sliding at all contacts. For each contact, the frictional force is $\langle F_i^s \rangle$ and the corresponding slip displacement is $\left(\Delta U_i^s\right)^{slip}$. The number of all contacts is N_c. Thus, frictional energy can be expressed as:

$$E_\mu = \sum_{N_c} \left(\langle F_i^s \rangle \left(\Delta U_i^s\right)^{slip} \right) \tag{5}$$

Kinetic energy (E_k) is the sum of the kinetic energy of the particle system, containing both translational and rotational motion. For each particle, the inertial mass is m_i, the inertial tensor is $\mathbf{I}_i$, the translational velocity is $\boldsymbol{v}_i$ and the rotational velocity is $\boldsymbol{\omega}_i$. The number of particles is N_p. Thus, kinetic energy can be expressed as:

$$E_k = \sum_{N_p} (m_i \boldsymbol{v_i}^2 + \mathbf{I}_i \boldsymbol{\omega}_i \cdot \boldsymbol{\omega}_i)/2 \tag{6}$$

Strain energy (E_s) is the total strain energy stored in all contacts. For a linear contact model, the normal and shear stiffnesses are k^n and k^s, respectively and the normal and shear contact forces are F_i^n and F_i^s, respectively. The number of all contacts is N_c. Thus, strain energy can be expressed as:

$$E_s = \sum_{N_c} (|F_i^n|^2/k^n + |F_i^s|^2/k^s)/2 \qquad (7)$$

The total energy (E_t) is the sum of bond energy, frictional energy, kinetic energy and strain energy. The energy ratio (R) is the ratio of total energy to boundary energy. The relation is denoted as:

$$R = E_t/E_w = (E_{pb} + E_\mu + E_k + E_s)/E_w \qquad (8)$$

The built-in FISH functions of PFC are used to monitor the release of energy in the loading process, with the results listed in Table 4. At low loading rates (such as 0.05/s and 0. 5/s), the change in loading rate has little effect on the test results. However, as the loading rate increases (> 5/s), the loading conditions become dynamic and the various energy components vary broadly. In this state, the boundary energy and kinetic energy increase with an increase in loading rate. Frictional energy also increases with the increase in loading rate except for the case of a 30° joint, where frictional energy decreases for a strain rate of 5/s. This phenomenon is related to the energy used in the propagation of cracks (seen in Fig. 7c).

Among the proportional contributions to total energy, frictional energy comprises the largest component, which illustrates that friction is the main effect controlling residual strength instead of the intrinsic strength mobilized post-peak. When the loading rate is greater than 5/s, the kinetic energy changes from zero to a positive value. Here we find another useful index describing the transition from static to dynamic loading.

The curves of energy ratio versus loading rate for each group are shown in Fig. 9. For intact specimens, energy ratio decreases gradually with an increase in loading rate. This implies that energy loss gradually increases with an increase in the loading rate. At high loading rates, boundary energy increases faster than the total energy because the failing part of specimens has already shed kinetic energy, with frictional dissipation occurring on the boundary walls and in the specimens. Moreover, an increase in the loading rate has little effect on the energy ratio in the case of fractures inclined at 45° and 60°. When the loading rate increases from 0.5/s to 5/s for the 30° joint, there is a

Table 4 Energy statistics for groups of numerical experiments

Joint angle	Strain rate (s^{-1})	Boundary energy E_w (N·m)	Bond energy E_{pb} (N·m)	Frictional energy E_μ (N·m)	Kinetic energy E_k (N·m)	Strain energy E_s (N·m)	Total energy E_t (N·m)
Intact	0.05	235.86	10.68	80.22	0.00	17.87	108.77
	0.5	235.70	10.54	79.23	0.00	17.97	107.75
	5	255.46	10.10	80.96	0.03	19.09	110.18
	10	274.64	11.04	83.06	0.08	20.39	114.57
	15	289.31	10.71	83.38	0.16	20.53	114.77
30°	0.05	262.27	20.84	123.85	0.00	27.47	172.17
	0.5	263.40	20.76	124.24	0.00	27.52	172.53
	5	237.13	10.86	89.68	0.05	20.04	120.62
	10	240.33	13.61	78.15	0.10	25.01	116.87
	15	248.68	13.58	79.11	0.15	24.67	117.51
45°	0.05	146.82	5.99	57.74	0.00	10.21	73.93
	0.5	147.22	6.02	57.81	0.00	10.23	74.07
	5	151.08	6.08	58.66	0.03	10.15	74.91
	10	156.07	6.27	59.86	0.09	10.30	76.52
	15	160.26	6.61	60.24	0.17	10.60	77.61
60°	0.05	88.36	2.27	37.22	0.00	5.11	44.6
	0.5	88.51	2.28	37.25	0.00	5.12	44.65
	5	89.95	2.32	37.48	0.02	5.17	44.99
	10	91.98	2.35	37.98	0.09	5.20	45.62
	15	94.00	2.48	38.07	0.19	5.36	46.1
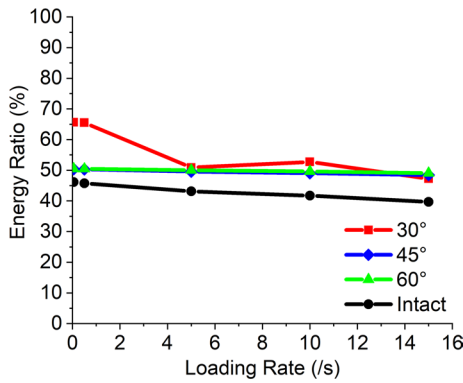
Fig. 9 Energy ratio curves for intact and jointed specimens under various loading rates

substantial reduction in energy ratio with this indicating a transition in failure modes.

Blanton (1981) built a dynamic representation of the testing apparatus to analyze strain rate effects by introducing a dashpot for damping. He noted that oscillations present in the displacement–time curves are due to the inertial term. The oscillations are damped-out at slow rates but the increased influence of the inertial term at high rates amplifies the amplitude of the oscillations. Local damping in PFC is used to dampen accelerating motions and maintain quasistatic equilibrium for the system. The effect of local damping is similar to the manifestation of the dashpot noted by Blanton (1981). Boundary energy noted in Fig. 9 is not equivalent to the total energy with the remainder of the boundary energy dissipated by local damping. As the energy rate decreases, the proportion of damping-to-dissipated energy increases along with an increase in loading rate. At high loading rate, the accelerating motion cannot be completely damped

out, so the kinetic energy turns positive from zero and the stress–strain curves shown in Fig. 4 exhibit oscillations.

4 Rate sensitivity of smooth joint model parameters

Rate sensitivity of the micro-parameters defining the SJM is a vital issue in determining the main factors affecting the failure modes of jointed rock at various loading rates. In the unbonded mode, the main micro-parameters of the SJM include normal stiffness (k_n, per unit area), shear stiffness (k_s, per unit area), and friction coefficient (μ). The ratio of k_n to k_s which defines the ratio of axial and lateral deformations of the rock joint is also considered in this section. Jointed specimens with joint angles of 30° and 45° are chosen for further discussion in this section. Loading rates between 0.5/s and 5/s represent test values representing the dynamic loading condition. Hence, three typical loading rates (0.5/s, 5/s, 15/s) are adopted from the triaxial compression numerical tests. The values of the various parameters of the SJM discussed in this section are listed in Table 5 with other parameters reported in Table 2.

4.1 Effect of joint friction coefficient (μ) of the smooth joint

The influence of the joint friction coefficient is investigated by varying its value across a range of five representative values (0.15, 0.3, 0.5, 0.8, 1.0). As shown in Fig. 10a, b, peak strength increases with an increase in joint friction coefficient while it remains below the threshold magnitude of ~0.5.

Table 5 List of micro-parameters of the smooth joint model (SJM) for rate sensitivity analysis

Joint angle (°)	Loading rate (/s)	Friction coefficient	Normal stiffness (GPa/m)	Shear stiffness (GPa/m)	Stiffness ratio
30	0.5	0.15	1260	840	10:1
45	5	0.3	630	420	5:1
	15	0.5	420	280	1:1
		0.8	315	210	1:5
		1.0	252	168	1:10
			126	84	
			50.4	33.6	
			25.2	16.8	

Fig. 10 Rate sensitivity of joint friction coefficient on macro-mechanical properties of jointed rock for joint inclinations of 30° and 45°: (1) Peak strength at joint inclinations of 30° (**a**) and 45° (**b**); (2) Elastic modulus for joint inclinations of 30° (**c**) and 45° (**d**); (3) Poisson's ratio for joint inclinations of 30° (**e**) and 45° (**f**)
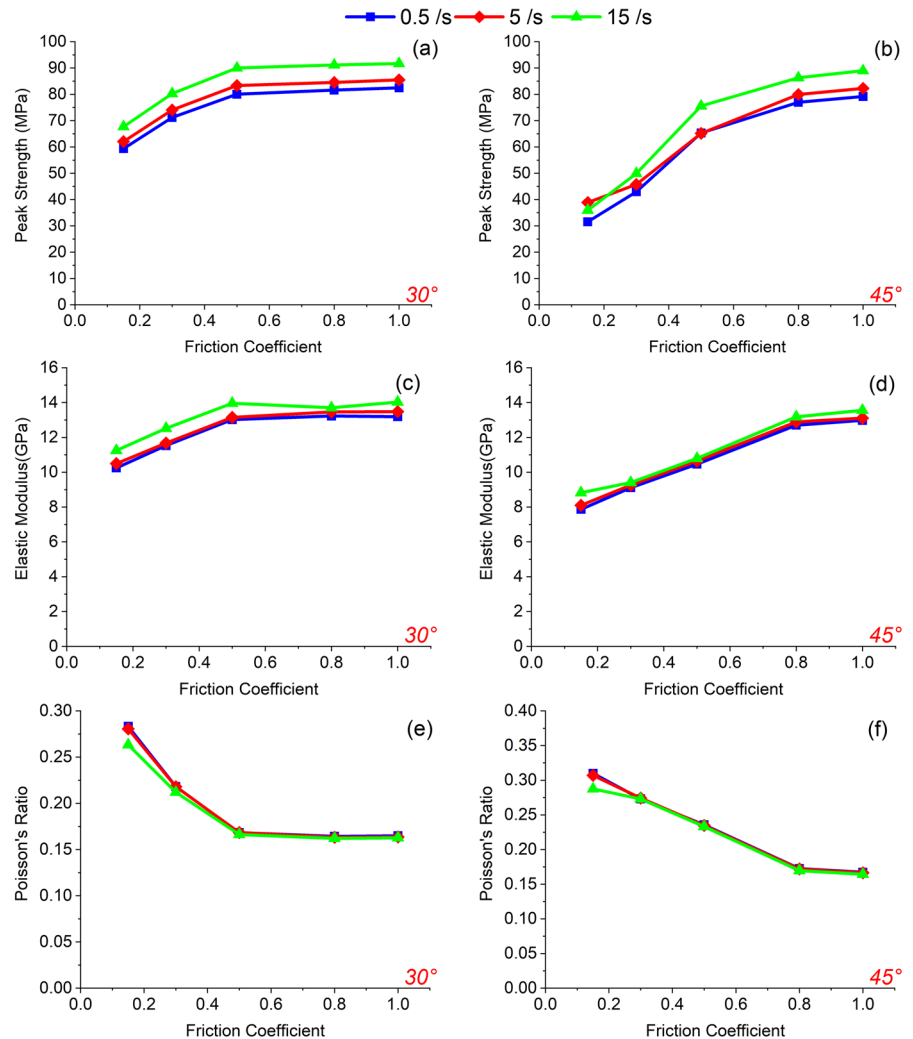
Change in peak strength occurs only slowly (for 45°) or is even absent (for 30°) when friction coefficient is > 0.5. With an increase in the friction coefficient, sliding along the joint surface become increasingly more difficult with the intact rock accommodating the increase in applied stress. However, after the friction coefficient increases to a defined magnitude, the growth trend in the load that the rock mass can withstand gradually slows and even arrests. Thus, a larger joint friction coefficient can clearly enhance the integrity of a specimen. Regardless, the peak intensity curves under these three loading rates show a consistent trend that an increase in loading rate gradually increases the intensity of the peak. An increase in joint friction coefficient has only a minor influence on this

trend for the case of a 30° joint with the increasing trend more obvious for that at 45°.

As shown in Fig. 10c, d, elastic modulus also tends to increase with an increase in friction coefficient. It appears that a friction coefficient of ~ 0.5 is a critical value to present loading rate effects. When it is below 0.5, the curves of elastic modulus for the three loading rates are almost parallel or overlap; and this tendency changes slowly when it is above 0.5.

To the contrary, as shown in Fig. 10e, f Poisson's ratio decreases with an increase in friction coefficient. When the friction coefficient increases to a threshold magnitude, Poisson's ratio decreases only slowly and then remains constant. For a low friction coefficient, an increase in the loading rate decreases the value of Poisson's ratio. As the friction coefficient increases to

a certain value (0.5 for 30° and 0.3 for 45°), the three curves showing Poisson's ratio for the three loading rates are nearly coincident.

4.2 Effect of stiffness of the smooth joint model

The effect of normal and shear stiffness of a smooth joint is investigated by separately reducing one stiffness value by a factor of 1, 2, 3, 5, 10, 25 and then 50 while keeping the other o constant.

4.2.1 Effect of normal stiffness

A normal stiffness (Table 2) of 1260 GPa/m per unit area is used as a base value for the varied reduction. In addition, the corresponding reduced magnitudes are shown in the fourth row of Table 5. As shown in Fig. 11a, b, with an increase in normal stiffness, peak strength remains nearly unchanged, but elastic modulus and Poisson's ratio each increases nonlinearly before eventually becoming invariant. As shown in Fig. 11c–f, when the normal stiffness is lower than 250 GPa/m per unit area, the increase in elastic modulus and Poisson's ratio is more pronounced. Along with an increase in normal stiffness, an increase in loading rate has a slight influence on the peak strength, elastic modulus, and the Poisson's ratio.

4.2.2 Effect of shear stiffness

On the basis of the value of 840 GPa/m in Table 1, the shear stiffness per unit area of the SJM is reduced as shown in the fifth row of Table 5. With the increase in shear stiffness, all of peak strength (Fig. 12a, b), elastic modulus (Fig. 12c, d), and Poisson's ratio (Fig. 12e, f) change imperceptibly. In comparison to the impact of a change in normal stiffness, the effect of shear stiffness can be essentially ignored in its impact on the macroscopic strength and deformation characteristics of the rock mass. It is also noted that the impact of shear stiffness at different loading rates on peak strength, elastic modulus and Poisson's ratio is minimal.

4.2.3 Effect of the ratio of normal to shear stiffness

The values of the ratio between normal and shear stiffness used in this section are listed in the sixth row of Table 5 when the shear stiffness is fixed at

840 GPa/m per unit area. As shown in Fig. 13a, b, in response to an increase in the stiffness ratio, peak strength remains constant while the joint is inclined at 30°, but decreases for a joint at 45° before the stiffness ratio increases to 1. As shown in Fig. 13c–f, with an increase in the stiffness ratio, both elastic modulus and Poisson's ratio increase, but this trend gradually weakens with the continued increase in stiffness ratio. When the stiffness ratio is less than 1, the elastic modulus and Poisson's ratio grow rapidly with an increase in the stiffness ratio, but they change only slowly when the stiffness ratio is > 1. With an increase in the ratio between normal and shear stiffness, the increase of loading rate has a slight influence on the peak strength, elastic modulus and Poisson's ratio.

4.3 Evaluation of rate sensitivity

Changes in four parameters representing the smooth joint model exert various influences on the rate sensitivity of the numerical specimens. Peak strength, elastic modulus and Poisson ratio are chosen as indicators of response sensitivity, and the evaluated results are listed in Table 6. Change in friction coefficient exerts a strong effect on rate sensitivity of both the elastic modulus and Poisson ratio, but only a slight change in peak strength. For changes in stiffness, normal stiffness has the most significant effect on rate sensitivity of the macroscopic mechanical properties. Based on the evaluated results, we conclude that the influence of these parameters on rate sensitivity of the macroscopic mechanical properties of rocks is in the order: Friction coefficient > Normal stiffness > Stiffness ratio > Shear stiffness.

5 Conclusions

Loading rates exert a significant effect on the strength of jointed rock masses and are an important issue in rock engineering. This paper reports a series of calibrated numerical experiments to study the micromechanical behavior of rock specimens containing fractures at three inclinations to the stress-field and subject to varied loading rates. The reported results can be extended to field scale since they indicate the nature of rock behaviour in the presence of a fracture and for different loading rates. Several conclusions are drawn:
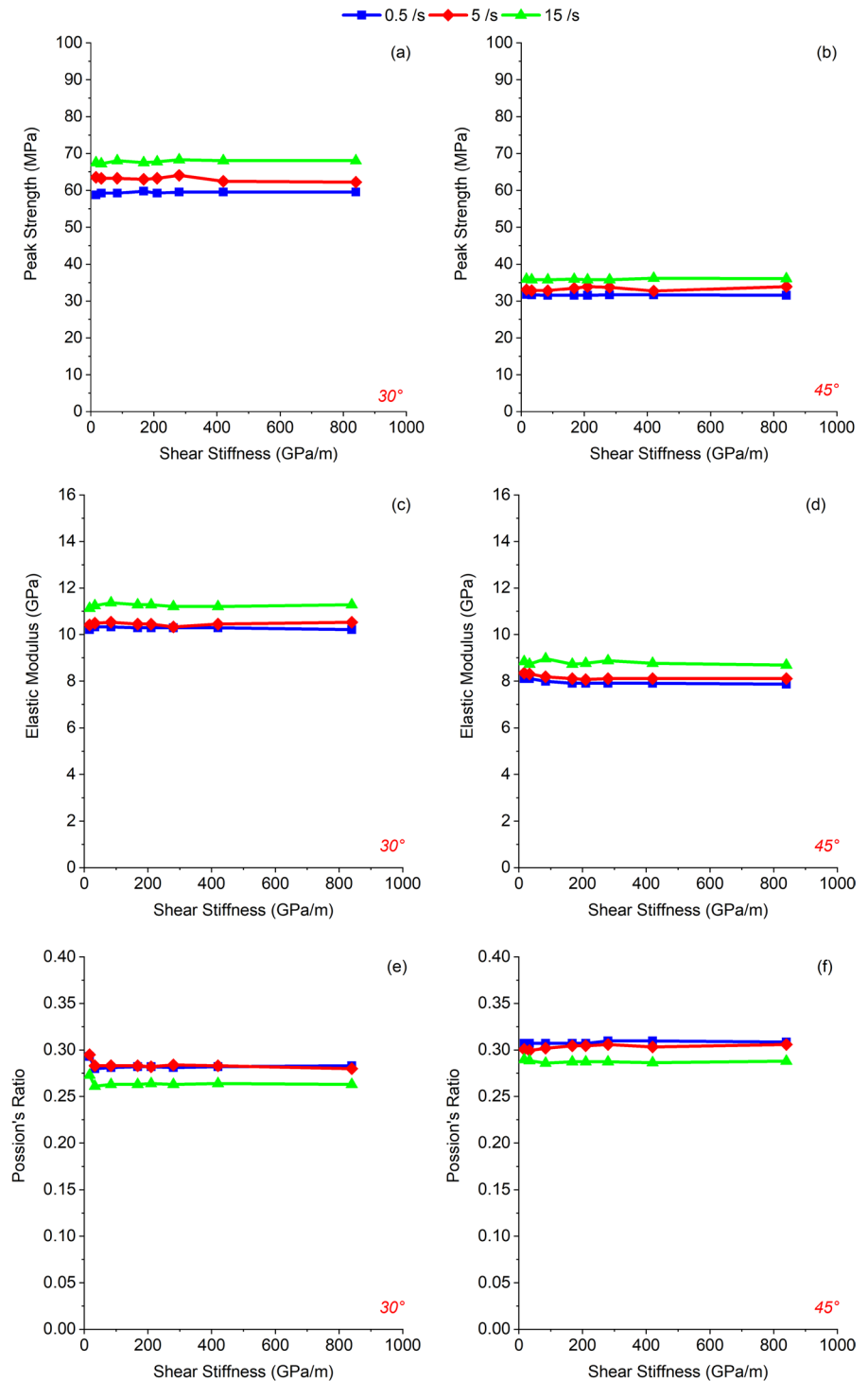
Fig. 11 Rate sensitivity of normal stiffness of the smooth joint model on macro-mechanical properties of jointed rock for joint inclination angles of 30° and 45°: (1) Peak strength for joint inclination angles of 30° (**a**) and 45° (**b**); (2) Elastic modulus for joint inclination angles of 30° (**c**) and 45° (**d**); (3) Poisson's ratio for joint inclination angles of 30° (**e**) and 45° (**f**)
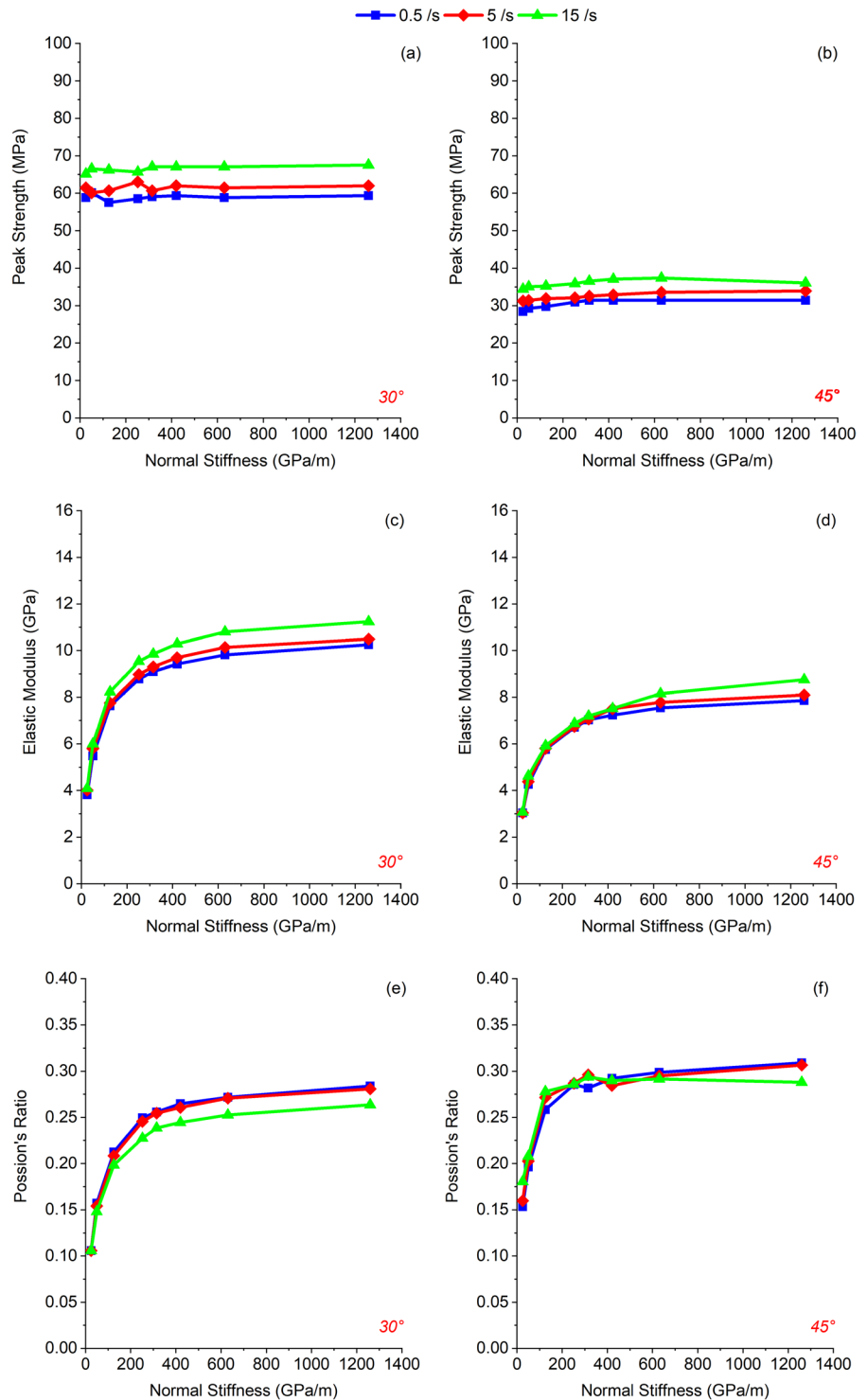
1. For all rock specimens, peak strength, and elastic modulus both increase with increased loading rate while Poisson ratio decreases. The damping of dissipated energy reflects the effects of inertia on the specimens at different loading rates.

Fig. 12 Rate sensitivity of shear stiffness of smooth joint model on macro mechanical properties of jointed rock at the joint inclination angles of 30° and 45°: (1) Peak strength for joint inclination angles of 30° (**a**) and 45° (**b**); (2) Elastic modulus at joint inclination angles of 30° (**c**) and 45° (**d**); (3) Poisson's ratio at joint inclination angles of 30° (**e**) and 45° (**f**)

2. Two features of the numerical results indicate that a critical value of strain rate exists in the interval from 0.5/s to 5/s, which changes the loading state from static to dynamic loading. When the loading rate is greater than 5/s, a step increase in the stress–strain curve is observed, which is charac-

Fig. 13 Rate sensitivity of stiffness ratio in the smooth joint model on macro mechanical properties of joint rock at the joint inclination angles of 30° and 45°: (1) Peak Strength at joint inclination angles of 30° (**a**) and 45° (**b**); (2) Elastic Modulus at joint inclination angles of 30° (**c**) and 45° (**d**); (3) Poisson's Ratio at joint inclination angles of 30° (**e**) and 45° (**f**)
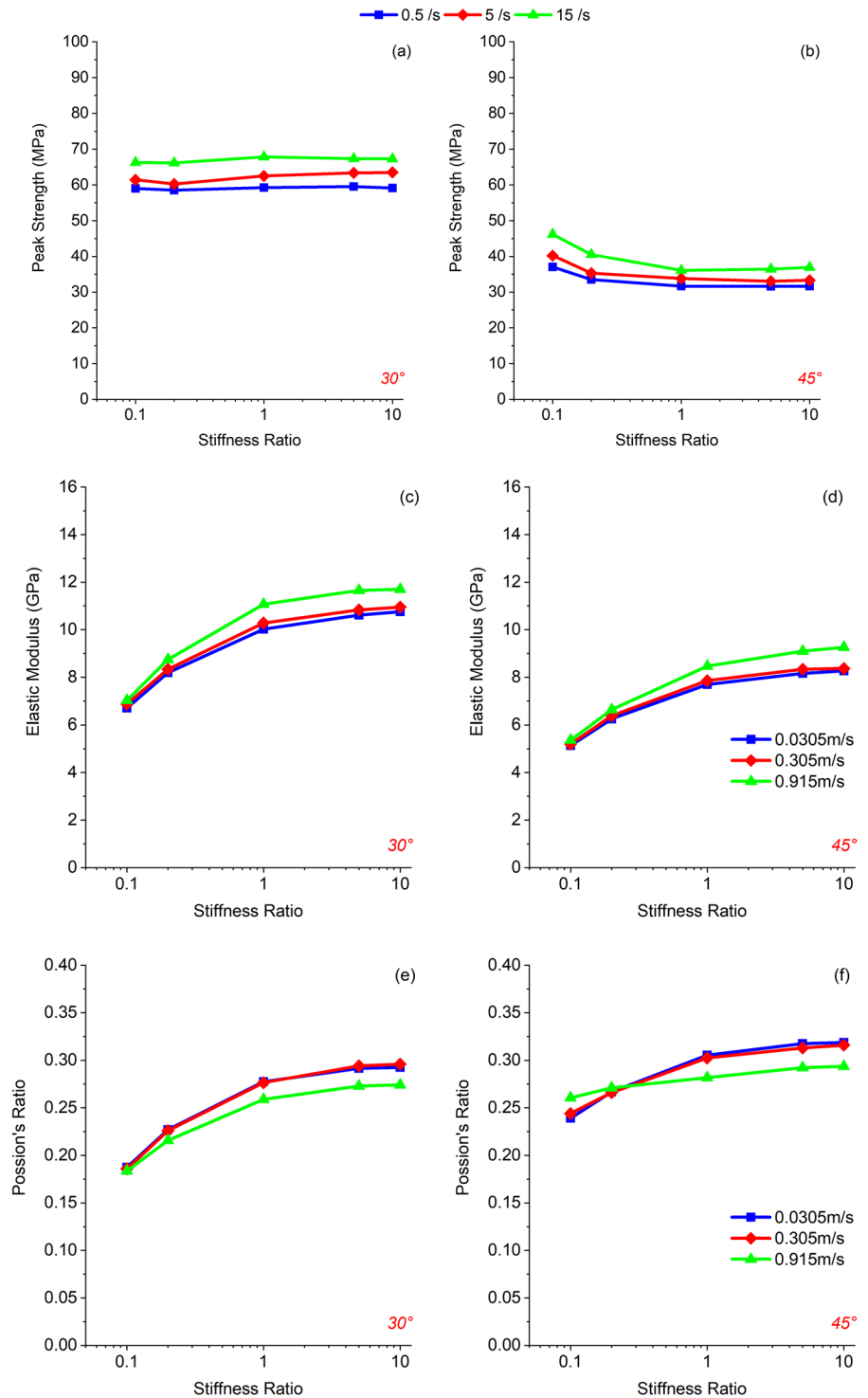
teristic of the onset of dynamic loading conditions. According to an energy response analysis, the kinetic energy also changes from zero to a positive value. This positive kinetic energy implies that inertial forces exert a significant

Table 6 Rate sensitivity of the parameters defining a smooth joint model

Rate Sensitivity	Friction Coefficient	Normal Stiffness	Shear Stiffness	Stiffness Ratio
Peak Strength	·	·	·	○
Elastic Modulus	●	●	·	·
Poisson's Ratio	●	·	○	●

Strong ● Slight · None ○

influence on the response of the specimens at high strain rates.

3. Fluctuations in the stress–strain curves in specimens with joints inclined at both 45° and 60° are more severe than those for intact specimens. This illustrates that the jointed specimens are more sensitive to a change in the loading rate than the intact specimens. This is consistent with the results of the physical tests.

4. The intact specimens fail in splitting mode with the jointed specimens (45° and 60°) failing in shear sliding mode. These failure modes do not change with increasing load rate. However, for specimens with a joint inclined at 30°, that remains mechanically locked, loading rate has a significant effect on the failure mode. When the loading rate is faster than 5/s, the specimens fail in combined conical fracturing and sliding instead of sliding only. The monitoring of energy ratio also reflects the change in failure mode with a clear transition occurring from 0.5/s to 5/s.

5. From rate sensitivity analysis of the microparameters defining the SJM, the influence of these parameters on the macroscopic mechanical properties of the rock joint is in the order: Friction coefficient > Normal stiffness > Stiffness ratio > Shear stiffness. The joint friction coefficient is the main rate dependent factor controlling behavior and may be an important factor in defining loading rate effects.

Declarations

Competing interests The authors declare that they have no conflict of interest.

References

Bahaaddini MP, Hagan P, Mitra R, Hebblewhite BR (2016) Numerical study of the mechanical behavior of nonpersistent jointed rock masses. Int J Geomech 16(1):1. https://doi.org/10.1061/(Asce)Gm.1943-5622.0000510

Blanton TL (1981) Effect of strain rates from 10–2 to 10-Sec-1 in triaxial compression tests on 3 rocks. Int J Rock Mech Min Sci 18(1):47–62. https://doi.org/10.1016/0148-9062(81)90265-5

Chen X, Zhang FS, Cheng C (2018) Numerical study on effect of joint strength mobilization on behavior of rock masses with large nonpersistent joints under uniaxial compression. Int J Geomech 18(11):1. https://doi.org/10.1061/(ASCE)GM.1943-5622.0001260

Chiu CC, Wang TT, Weng MC, Huang TH (2013) Modeling the anisotropic behavior of jointed rock mass using a modified smooth-joint model. Int J Rock Mech Min Sci 62:14–22. https://doi.org/10.1016/j.ijrmms.2013.03.011

Dieterich JH (1972) Time-dependent friction in rocks. J Geophys Res 77(20):3690–3697. https://doi.org/10.1029/JB077i020p03690

Dieterich JH (1978) Time-dependent friction and the mechanics of stick-slip. Pure Appl Geophys 116(4–5):790–806. https://doi.org/10.1007/bf00876539

Duan K, Kwok CY, Pierce M (2016) Discrete element method modeling of inherently anisotropic rocks under uniaxial compression loading. Int J Numer Anal Methods Geomech 40(8):1150–1183. https://doi.org/10.1002/nag.2476

Fahimifar A (1996) Effects of strain rate on rock joint deformation. In: Proceedings of 7th Australia New Zealand conference on geomech: geomech in a changing world, pp 75–79

Fahimifar A (1997) Effects of strain rate on the stress-strain behavior of discontinuous rock. Iran J Sci Technol 21(1):35–46

FahimifarA SH (2005) Effect of time on the stress–strain behaviour of a single rock joint. Bull Eng Geol Environ 64(4):383–396. https://doi.org/10.1007/s10064-005-0003-4

Fairhurst CE, Hudson JA (1999) Draft ISRM suggested method for the complete stress-strain curve for intact rock in uniaxial compression. Int J Rock Mech Min Sci 36(3):279–289

Gao G, Meguid MA, Chouinard LE (2020) On the role of pre-existing discontinuities on the micromechanical behavior of confined rock samples: a numerical study. Acta Geotech. https://doi.org/10.1007/s11440-020-01037-0

Hu W, Kwok C, Duan K, Wang T (2018) Parametric study of the smooth-joint contact model on the mechanical behavior of jointed rock. Int J Numer Anal Methods Geomech 42(2):358–376. https://doi.org/10.1002/nag.2751

Hu W, Wang T, Kwok C, Duan K (2016) The effect of smooth-joint parameters on the mechanical behavior of jointed rock. In: Proceedings of 50th U.S rock mech/geomech symposium: ARMA

Huang D, Wang JF, Liu S (2015) A comprehensive study on the smooth joint model in DEM simulation of jointed rock masses. Granul Matter 17(6):775–791. https://doi.org/10.1007/s10035-015-0594-9

Huang SB, Yao N, Ye YC, Cui XZ (2019) Strength and failure characteristics of rocklike material containing a large-opening crack under uniaxial compression: experimental and numerical studies. Int J Geomech 19(8):1. https://doi.org/10.1061/(ASCE)GM.1943-5622.0001477

Itasca (2008) Theory and Background. PFC2D (particle flow code in 2 dimensions), V4.0

Ivars DM, Pierce ME, Darcel C, Montes JR, Potyondy DO, Young RP, Cundall PA (2011) The synthetic rock mass approach for jointed rock mass modelling. Int J Rock Mech Min Sci 48(2):219–244. https://doi.org/10.1016/j.ijrmms.2010.11.014

Jackson K, Kingman SW, Whittles DN, Lowndes IS, Reddish DJ (2008) The effect of strain rate on the breakage behaviour of rock. Arch Min Sci 53(1):3–22

Jaeger JC, Cook NGW, Zimmerman R (2007) Fundamental of rock mechanics, 4th ed

Lajtai EZ, Duncan EJS, Carter BJ (1991) The effect of strain rate on rock strength. Rock Mech Rock Eng 24(2):99–109. https://doi.org/10.1007/Bf01032501

Lambert C, Coll C (2014) Discrete modeling of rock joints with a smooth-joint contact model. J Rock Mech Geotech Eng 6(1):1–12. https://doi.org/10.1016/j.jrmge.2013.12.003

Li HB, Li JC, Liu B, Li JR, Li SQ, Xia X (2013) Direct tension test for rock material under different strain rates at quasi-static loads. Rock Mech Rock Eng 46(5):1247–1254. https://doi.org/10.1007/s00603-013-0406-7

Logan JM (1970) Triaxial compression testing at intermediate strain rates. Brit J Psychiat 54(9):2464–2478

Mehranpour MH, Kulatilake PHSW (2017) Improvements for the smooth joint contact model of the particle flow code and its applications. Comput Geotech 87:163–177

Olsson WA (1991) The Compressive Strength of Tuff as a Function of Strain Rate from 10–6 to 103/Sec. Int J Rock Mech Min Sci 28(1):115–118. https://doi.org/10.1016/0148-9062(91)93241-W

Potyondy DO, Cundall PA (2004) A bonded-particle model for rock. Int J Rock Mech Min Sci 41(8):1329–1364. https://doi.org/10.1016/j.ijrmms.2004.09.011

Qi CZ, Wang MY, Qian QH (2009) Strain-rate effects on the strength and fragmentation size of rocks. Int J Impact Eng 36(12):1355–1364. https://doi.org/10.1016/j.ijimpeng.2009.04.008

Schneider H (1977) The time dependence of friction of rock joints. Bull IAEG 16(1):235–239. https://doi.org/10.1007/bf02591495

Scholz CH (1998) Earthquakes and friction laws. Nature 391(6662):37–42. https://doi.org/10.1038/34097

Sierakowski RL (1985) Dynamic effect in concrete materials. Springer, Netherlands

Swan GJ, Cook SB, Meehan R (1989) Strain rate effects in kimmeridge bay shale. Int J Rock Mech Min Sci 26(2):135–149. https://doi.org/10.1016/0148-9062(89)90002-8

Tarasov BG (1990) Simplified method for determining the extent to which strain rate affects the strength and energy capacity of rock fracture. Sov Min Sci 26(4):315–320. https://doi.org/10.1007/Bf02506510

Wang T, Xu DP, Elsworth D, Zhou WB (2016) Distinct element modeling of strength variation in jointed rock masses under uniaxial compression. Geomech Geophys Geo-Energy Geo-Resour 2(1):11–24. https://doi.org/10.1007/s40948-015-0018-7

Wang T, Zhou WB, Chen JH, Xiao X, Li Y, Zhao XY (2014) Simulation of hydraulic fracturing using particle flow method and application in a coal mine. Int J Coal Geol 121:1–13. https://doi.org/10.1016/j.coal.2013.10.012

Wang T, Hu WR, Elsworth D, Zhou Y, Zhou WB, Zhao XY, Zhao LZ (2017) The effect of natural fractures on hydraulic fracturing propagation in coal seams. J Pet Sci Eng 150:180–190. https://doi.org/10.1016/j.petrol.2016.12.009

Zhang XP, Wong LNY (2014) Choosing a proper loading rate for bonded-particle model of intact rock. Int J Fract 189(2):163–179. https://doi.org/10.1007/s10704-014-9968-y

Zhang Y, Ren F, Zhao X (2017) Characterization of joint set effect on rock pillars using synthetic rock mass numerical method. Int J Geomech 17(3):1. https://doi.org/10.1061/(Asce)Gm.1943-5622.0000756

Zou C, Suo Y, Liu K, Cheng Y, Li J (2022) Feasibility of artificial materials in simulating rock failure based on rate-dependent brittleness indexes. Rock Mech Rock Eng. https://doi.org/10.1007/s00603-022-02902-y